

X-Ray Spectroscopy of SN 1006 with Suzaku

Hiroya YAMAGUCHI,¹ Katsuji KOYAMA,¹ Satoru KATSUDA,² Hiroshi NAKAJIMA,² John P. HUGHES,³
Aya BAMBA,⁴ Junko S. HIRAGA,⁵ Koji MORI,⁶ Masanobu OZAKI,⁴ and Takeshi Go TSURU¹

¹*Department of Physics, Kyoto University, Kitashirakawa-oiwake-cho, Sakyo-ku, Kyoto 606-8502*
hiroya@cr.scphys.kyoto-u.ac.jp

²*Department of Earth and Space Science, Osaka University, 1-1 Machikaneyama, Toyonaka, Osaka 560-0043*

³*Department of Physics and Astronomy, Rutgers University, 136 Frelinghuysen Road, Piscataway, NJ 08854-8019, U.S.A.*

⁴*Institute of Space and Astronautical Science, JAXA, 3-1-1 Yoshinodai, Sagami-hara, Kanagawa 229-8510*

⁵*RIKEN (The Institute of Physical and Chemical Research), 2-1 Hirosawa, Wako, Saitama 351-0198*

⁶*Department of Applied Physics, University of Miyazaki, 1-1 Gakuen Kibana-dai Nishi Miyazaki, 889-2192*

(Received 2007 May 6; accepted 2007 June 12)

Abstract

We report on observations of SN 1006 with Suzaku. We firmly detected K-shell emission from Fe, for the first time, and found that the Fe ionization state is quite low. The broad-band spectrum extracted from southeast of the remnant was well-fitted with a model consisting of three optically thin thermal non-equilibrium ionization plasmas and a power-law component. Two of the thermal models are highly overabundant in heavy elements, and hence are likely due to ejecta. These components have different ionization parameters, $n_e t \sim 1.4 \times 10^{10} \text{ cm}^{-3} \text{ s}$ and $n_e t \sim 7.7 \times 10^8 \text{ cm}^{-3} \text{ s}$; it is the later one that produces Fe-K emission. This suggests that Fe has been heated by reverse shock more recently than the other elements, consistent with a picture where the ejecta are stratified by composition with Fe in the interior. On the other hand, the third thermal component is assumed to be solar abundance, and we associate it with emission from the interstellar medium (ISM). The electron temperature ($kT_e \sim 0.5 \text{ keV}$) is lower than that expected from the shock velocity, which suggests a lack of collisionless electron heating at the forward shock. The extremely low ionization parameter and extreme non-equilibrium state are due to the low density of the ambient medium.

Key words: Supernova Remnants: individual (SN 1006) — X-Rays: spectra

1. Introduction

Based on the historical record, SN 1006 is widely regarded to be one of the Galactic type Ia supernova remnants (SNRs) similar to Tycho's SNR (Schaefer 1996). The current supernova (SN) models predict that Fe production in type Ia SNe is far larger than that of core-collapse SNe (e.g., Nomoto et al. 1984; Iwamoto et al. 1999). Therefore, measuring the Fe abundance is one of the essential clues to classify the SN type of any specific remnant. The K-shell X-ray emission lines from ionized Fe offer the most direct information for abundance determination. In fact, strong Fe-K α lines had been observed from Tycho's SNR (e.g., Hwang et al. 1998; Decourchelle et al. 2001).

In SN 1006, Vink et al. (2000) suggested the possible presence of an Fe-K emission line at $6.3 \pm 0.2 \text{ keV}$ from the BeppoSAX MECS spectrum. However, the detection was not clear, because the energy resolution of the MECS (a gas scintillation counter) was relatively poor (FWHM $\sim 500 \text{ eV}$ @ 6 keV). Other recent X-ray missions, Chandra and XMM-Newton, have not succeeded in detecting an Fe-K line. Cold Fe in the interior of SN 1006 is known to exist based on ultraviolet absorption studies. Blue and red-shifted Fe II absorption lines were detected in the spectra of background stars (Wu et al. 1993; Hamilton

et al. 1997; Winkler et al. 2005), and interpreted as being due to unshocked Fe in the interior of the remnant. These results show that portions of the Fe-rich ejecta are still expanding freely, and have not yet been overrun by the reverse shock. However the amount of Fe inferred in these studies ($< 0.16 M_\odot$) is much less than the amount ($0.6\text{--}0.8 M_\odot$) predicted to be produced in the thermonuclear disintegration of a $\sim 1.4 M_\odot$ white dwarf.

In the early phases of supernova remnant evolution, even the shock-heated plasma is far from thermal equilibrium in terms of either the ionization or particle (electron and ion) temperatures. The ionization age, a key diagnostic of the non-equilibrium ionization (NEI) state, is defined as $n_e t$, the product of the electron density and the time since the gas was heated. Typically, $n_e t$ is required to be $\geq 10^{12} \text{ cm}^{-3} \text{ s}$ for full ionization equilibrium (Masai 1984). The thermal X-ray spectrum of SN 1006 suggests an ionization timescale of $n_e t \sim 2 \times 10^9 \text{ cm}^{-3} \text{ s}$ (Vink et al. 2000), which is far from the full ionization equilibrium, and lower than nearly all other Galactic SNRs. The electron temperature at the northwest rim of the remnant has been estimated to be $kT_e \sim 0.7 \text{ keV}$ (Long et al. 2003) or $\sim 1.5 \text{ keV}$ (Vink et al. 2003). Since these values are much lower than the ion temperature expected from the shock velocity of $\sim 2980 \text{ km s}^{-1}$ (Ghavamian et al. 2002), non-equilibration of ion and electron temperatures is present

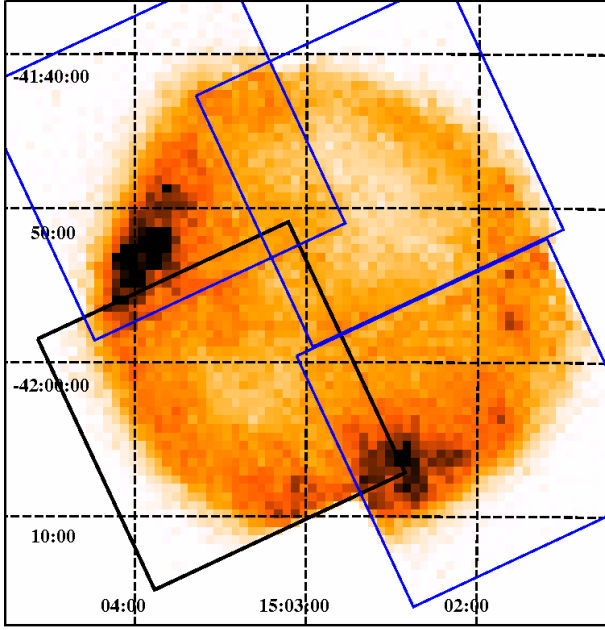


Fig. 1. XIS-BI mosaic image of SN 1006 in the 0.55–0.6 keV band. Exposure and vignetting effects are corrected. The coordinates (R.A. and Dec) are referred to epoch J2000.0. The black square shows the FOV of the XIS on the SE region of SN 1006 where this paper is concentrated. The blue squares show the FOVs on the other three quadrants (NE, NW, and SW).

in SN 1006 as well.

The extreme non-equilibrium state and high shock velocity are likely due to the low density of the ambient gas, because SN 1006 ($b = +14.6$) is further from the Galactic plane than other Galactic SNRs, such as Cas A ($b = -2.1$) and Tycho's SNR ($b = +1.4$). Although Kepler's SNR ($b = 6.8$) is nearly as far above the plane as SN1006 (when their respective distances are included), Kepler appears to be evolving into a dense circumstellar medium. Therefore, the evolutionary state of SN 1006 may be the lowest of these youngest Galactic SNRs, even though the real age is ~ 3 times older than the others.

In this paper, using the type Ia SNR, SN 1006, we consider the X-ray spectra to investigate this very early phase of SNR evolution. Suzaku (Mitsuda et al. 2007), with its high sensitivity for diffuse sources and spectroscopic resolution in the ~ 5 –10 keV energy range, is well-suited for this study.

We assume the distance to SN 1006 to be 6.8×10^{21} cm, following Winkler et al. (2003). The errors quoted in this paper represent the 90% confidence level, unless otherwise stated.

2. Observations and Data Reduction

Four pointings were made of SN 1006 with Suzaku during the performance verification (PV) phase. Suzaku has one Hard X-ray Detector (HXD; Takahashi et al. 2007, Kokubun et al. 2007), and four X-ray Imaging

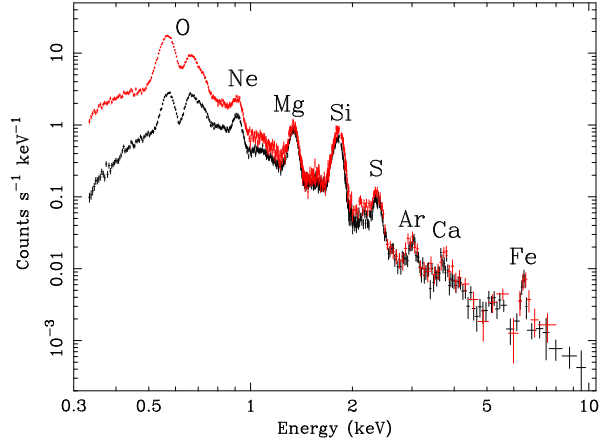


Fig. 2. Background-subtracted XIS spectra extracted from the whole SE quadrant (SN 1006 SE). The black and red points represent the FI and BI spectra, respectively.

Spectrometers (XIS; Koyama et al. 2007) each placed in the focal plane of an X-Ray Telescope (XRT; Serlemitsos et al. 2007). This paper reports on the imaging and spectral results obtained with the XIS. The XIS consist of three Front-Illuminated (FI) CCDs and one Back-Illuminated (BI) CCD. The advantages of the former are high detection efficiency and low background level in the energy band above ~ 5 keV, while the latter has significantly superior sensitivity in the 0.2–1.0 keV band with moderate energy resolution. All four XRTs are co-aligned to image the same region of the sky. The XIS were operated in the normal full-frame clocking mode with the editing mode of 3×3 or 5×5 .

We employed the cleaned revision 0.7 data, and used the HEADAS software version 6.0.4 and XSPEC version 11.3.2 for the data reduction and analysis. The X-ray data taken during low cut-off rigidity (≤ 6 GV) were excluded so as to minimize any possible uncertainty in the non X-ray background (NXB). The total effective exposure times after these screening were ~ 50 ks, for each of the pointings. The response matrix files (RMF) and ancillary response files (ARF) were made using xisrmfgen and xissarmfgen (Ishisaki et al. 2007) version 2006-10-17.

3. Overall Structure

3.1. Thin-Thermal Plasma Map

The field of view (FOV) of the XIS is $\sim 18' \times 18'$, and hence a four-point mosaic can completely cover SN 1006 (about $30'$ diameter). Since we intended to study the thermal plasma, we searched for the region of the remnant with the most prominent thermal emission. We hence made a mosaic image in the O VII $K\alpha$ line band (0.55–0.6 keV), because this line is a major component of the thermal plasma in SN 1006. The result is shown in figure 1. We can see bright emission in this band in the northeast (NE) and southwest (SW) regions of the remnant. However, these are dominated by non-thermal emission (Koyama et al. 1995), from which it is difficult to

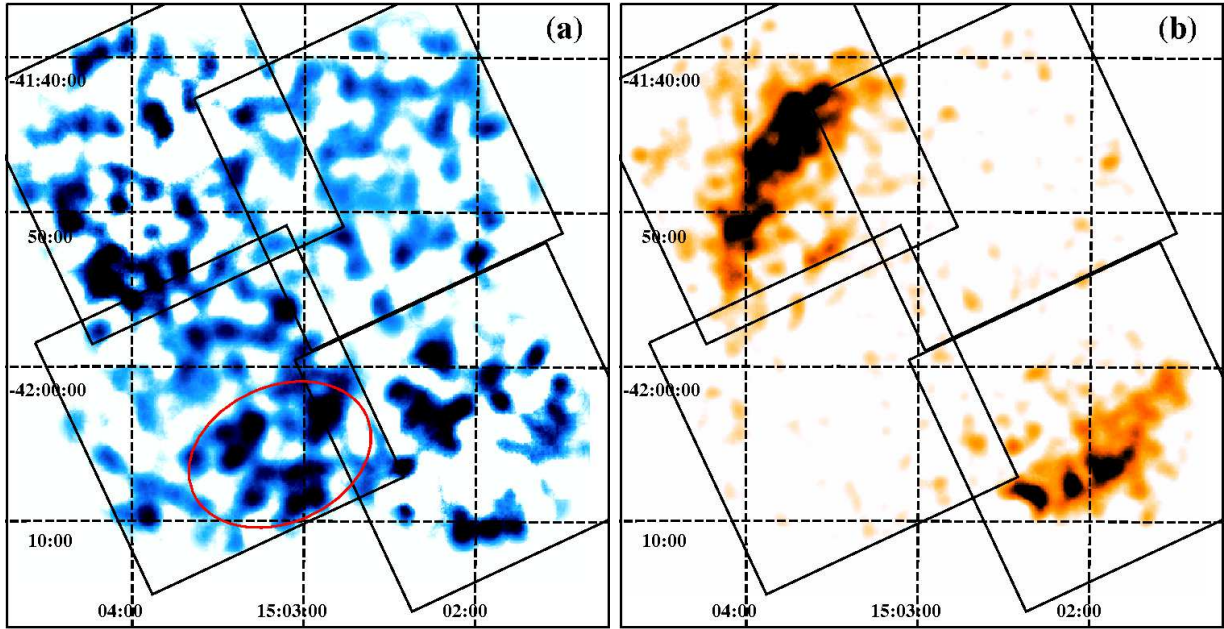


Fig. 3. XIS intensity map at the Fe-K α line (a: 6.33–6.53 keV band), from which the continuum flux at 6.1–6.3 keV band [shown in (b)] is subtracted. In both images, exposure and vignetting effects are corrected. The data from the three FIs are combined. Two corners of the calibration sources are removed. The black squares indicate each FOVs of the XIS. The red ellipse shows the region where we extracted the spectra for a detailed analysis.

extract thermal spectra. Other regions are dominated by thermal emission. In particular, as shown in figure 1, the southeast quadrant (here SN 1006 SE) is brighter than the northwest (NW). Therefore, our study concentrated on this region. The spectral results of non-thermal rims (NE and SW) are reported by Bamba et al. (2008), and those of the other regions (NW quadrant and the center of the remnant) will be reported in another paper in the future. The FOV of the XIS on SN 1006 SE is outlined by the black solid square in figure 1, which was observed on 2006 January 30 (Obs. ID=500016010).

3.2. Spectrum of the SN 1006 SE Region

We extracted the spectrum of the entire SN 1006 SE region, excluding the two corners in the FOV that contain calibration source emission. For the background, we used the North Ecliptic Pole (NEP) data (Obs. date = 2006 February 10, Obs. ID = 500026010, Exp. time = ~ 82 ks). Although we have been monitoring and correcting the increase of the Charge-Transfer Inefficiency (CTI) for the XIS (see Koyama et al. 2007), recovery of the energy resolution cannot be made. However, we can ignore the difference of the spectral resolution between the SN 1006 SE and NEP observations, because the latter observation was made only ten days after the former. To minimize the uncertainty due to the background subtraction, in particular that of NXB, we applied the same data-screening criteria to both the SN 1006 SE and NEP observations, and took background spectra from the same detector coordinates as the source regions after excluding point-like sources detected in the NEP data. The background-subtracted spectra are shown in figure 2. Since the data from the

three FIs are nearly identical, we merged those individual spectrum to improve the photon statistics.

As shown in figure 2, we found clear K-shell ($K\alpha$) lines from Ar, Ca, and Fe, for the first time. With a power-law plus Gaussian-line fit, we determined the line center energy of the Fe-K α to be ~ 6.43 keV. This energy constrains the Fe ionization state to be approximately Ne-like.

3.3. Iron Line Map

We show in figure 3a an image in a relatively narrow band (6.33–6.53 keV) that contains the Fe-K α line. This image was generated by subtracting the continuum flux at energies of 6.1–6.3 keV. (The image in this band is shown in figure 3b.)

We can see that the Fe-K α flux is enhanced at the southern part of the remnant (outlined in red with a ellipse), except for the NE and SW quadrants where the non-thermal emission is dominant. The mean surface brightness at 6.33–6.55 keV within the elliptical region is $8.5 (\pm 0.5) \times 10^{-9}$ photons $\text{cm}^{-2} \text{s}^{-1} \text{arcmin}^{-2}$, while that outside it (only in the SE and NW quadrants) is $4.6 (\pm 0.3) \times 10^{-9}$ photons $\text{cm}^{-2} \text{s}^{-1} \text{arcmin}^{-2}$. In order to study the thin-thermal spectrum with the best S/N ratio for Fe-K line, we extracted the X-ray spectrum from within the elliptical region, excluding the corner of the calibration sources. The background subtraction was made in the same way as that of the full-field spectrum. The results are given in figure 8. Hereafter, all detailed analyses are made using this spectrum.

Table 1. The center energies and widths of the emission lines.

Line	Center energy* (eV)	Width [†] (eV)
Mg-K α	1338 (1337–1340)	< 5.4
Si-K α	1815 (1813–1816)	40 (38–42)
S-K α	2361 (2355–2365)	60 (54–65)
Ar-K α	3010 (2991–3023)	< 50
Ca-K α	3692 (3668–3724)	< 57
Fe-K α	6430 (6409–6453)	< 60

* Errors (statistical only) are given in the parentheses (see text).

[†] One standard deviation (1σ).

3.4. Energy and Width of the Emission Lines

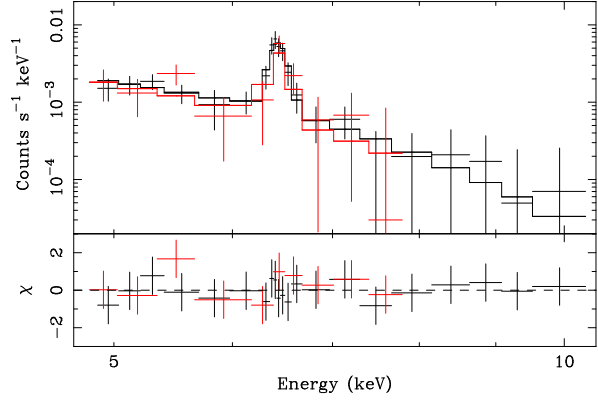
In order to study the line features, we fitted the spectra extracted from the elliptical region with a phenomenological model; a power-law for the continuum and Gaussians for the emission lines. The best-fit central energies and widths for the emission lines are shown in table 1. Since the absolute energy calibration error is $\pm 0.2\%$ above 1 keV (Koyama et al. 2007), the relevant elements are uniquely identified from the best-fit central energy. These are also listed in table 1. Except for Mg, the central energies are significantly lower than that of the respective He-like K α lines. We also note that the widths of the Gaussians identified with Si-K α and S-K α are significantly broader than the instrumental energy resolution at those energies. Figure 6a would help to compare the widths of the data with those of narrow lines. In subsection 4.3, we discuss this matter in detail.

4. Spectral Structure in the Narrow Bands

In order to study the plasma characteristics in relation to the various elements, we at first divided the spectrum into three representative energy bands: the 0.4–1.1 keV band for the O and Ne (light elements) lines, the 1.2–2.8 keV band for the Mg, Si, and S (medium elements) lines, and the 5–10 keV band for the Fe (heavy element) line. With the fitting to these individual band spectra, we constrained the plasmas including light, medium, and heavy elements separately.

4.1. The 5–10 keV Band Spectra

We fitted the 5–10 keV spectrum with a solar abundance (Anders and Grevesse 1989) VNEI model. Since the NEIvers 2.0 plasma code does not include K-shell emission lines for ions below the He-like state, we reverted to the NEIvers 1.1 code. If we fix the Fe abundance to be solar, then the model cannot reproduce the Fe-K α profile or flux, although the $\chi^2/\text{d.o.f.}$ of 25/28 is acceptable. Allowing the Fe abundance to be free results in a greatly improved best-fit $\chi^2/\text{d.o.f.}$ of 10/27. The best-fit kT_e , $n_e t$, and Fe abundance are 3.8 (1.7–26) keV, 6.1 (2.2–10) $\times 10^9 \text{ cm}^{-3} \text{ s}$, and 6.5 (> 1.9) solar, respectively. The Fe abundance is significantly enhanced relative to solar, even if the continuum flux in this band is assumed to be composed of

**Fig. 4.** XIS spectra in the 5–10 keV band with the VNEI model. The black and red data points represent the FI and BI spectra, respectively. In the BI spectrum, the energy band above 8 keV is ignored.

pure thermal emission. The best-fit spectrum is shown in figure 4.

4.2. The 0.4–1.1 keV Band Spectra

Figure 5 shows the 0.4–1.1 keV band spectra. This energy band includes K α lines of the light elements, with dominant emission from the oxygen K-shell line series. The spectra were fitted with a VNEI model, allowing the abundances of C, N, O, and Ne to be free parameters. Also, we let the abundances of Ca and Fe to be free, because the L-shell lines of these elements fall into this energy band (0.4–1.1 keV). Interstellar absorption was fixed to a hydrogen column density of $6.8 \times 10^{20} \text{ cm}^{-2}$ (Dubner et al. 2002). In the initial fits, we found a significant inconsistency between the FI and BI spectra near the energy of the O-edge (0.54 keV). This may be due to incomplete calibration information for the contamination layer on the optical blocking filter (OBF) of the XIS (Koyama et al. 2007). Since the calibration of the OBF contamination for the BI is more accurate than that for the FI, we decided to retain the BI data across this energy band and ignore the 0.5–0.63 keV band in the FI spectrum. The results are shown in figure 5a, with the best-fit temperature and ionization parameter of $kT_e = 0.58$ (0.56–0.59) keV and $n_e t = 6.7$ (6.6–6.8) $\times 10^9 \text{ cm}^{-3} \text{ s}$.

In figure 5a, we find an apparent disagreement between the data and model in the ~ 0.7 – 0.85 keV energy band. Usually, this energy band is dominated by the iron L-shell line transitions of $3s-2p$ (~ 730 eV) and $3d-2p$ (~ 830 eV) from Fe XVII. Although the fluxes of these two lines in NEI models are nearly equal over a wide range of plasma conditions, extrapolation to the extremely low ionization states that we see here in SN 1006 is quite uncertain. In particular, for the young Type Ia SNR E0509–67.5, Warren and Hughes (2004) found that the Fe L-shell emission was dominated by an emission from a line feature near 0.73 keV, which was not sufficiently strong in the spectral models and had to be included as a separate Gaussian component. Based on the strength of other Fe-L emission lines

and the weakness of O emission in E0509–67.5 the additional line feature at 0.73 keV was confidently associated with Fe-L emission.

Although we cannot eliminate the possibility that the residual comes from faint Fe-L emission, here we consider a different explanation. The best-fit spectral model of the oxygen lines are shown in figure 5b, in which the black and red solid lines are K-shell transitions from O VII and O VIII, respectively. In most astrophysical plasmas, the best-fit temperature of ~ 0.6 keV gives weak K-shell lines of O VII compared to those of O VIII. On the other hand, in lower temperature plasmas (e.g., $kT_e \sim 0.1 - 0.2$ keV) where the O VII K α line is dominant, the line fluxes decrease rapidly along the K-shell transition series (K $\alpha, \beta, \gamma, \delta, \epsilon, \zeta$, etc.). Therefore, K-shell lines in the higher transitions can be safely ignored, and hence conventional NEI codes do not include O VII K-shell transition lines higher than K δ . This is the reason that no oxygen line in the $\sim 0.7-0.85$ keV band is present in the best-fit model (figure 5b). In SN 1006, however, the ionization timescale is low, while kT_e is moderate, so the fluxes of higher level K-shell transitions from O VII may be relatively strong and cannot be ignored. To account for them we added Gaussians at 714 eV, 723 eV, and 730 eV to represent the O VII K δ , K ϵ , and K ζ lines, respectively. At a plasma temperature of 0.6 keV, the flux ratio of O VIII Ly ϵ to Ly δ predicted by the NEIvers 1.1 code is ~ 0.5 (see figure 5b). In the absence of a detailed calculation we merely assumed that the flux ratio of the O VII lines follow the same pattern, namely $K\epsilon/K\delta = K\zeta/K\epsilon = 0.5$. The best-fit results with these additional lines, see figure 5c, are a reasonably good fit. The additional artificial lines are also shown as the dotted lines in figure 5b. The temperature and ionization parameter are almost the same as those obtained without the additional higher K-shell transitions of O VII.

The best-fit intensity ratio of O VII K β to O VIII Ly α is ~ 1.4 , which is consistent with the result of the XMM-Newton/RGS observation of the X-ray knot localized at the NW rim of SN 1006 (Vink et al. 2003; O VII K β /O VIII Ly $\alpha \sim 1.6$). This agreement may justify our approach to include the K-lines manually. Also, this suggests that the O VII K-shell line series are key spectral components for all over the SN 1006 plasma.

4.3. The 1.2–2.8 keV Band Spectra

This band includes K-shell lines of medium-weight elements (Mg, Si, and S). As shown in table 1, we see can significant broadening of the Si and S K α lines. Therefore, the 1.2–2.8 keV band spectra cannot be reproduced with a single-component plasma model. In fact, we found significant disagreement between the data and model around the Si-K α and S-K α lines (figure 6a) in the one-component VNEI fits. The lack of data in the 1.83–1.85 keV band is due to current calibration errors of the XIS; there is a small gap in energy (~ 10 eV) at the Si K-edge, which is not implemented in the current response function. The apparent line broadening of the Si K α line, however, is much larger (~ 40 eV) than this gap. Therefore, the dis-

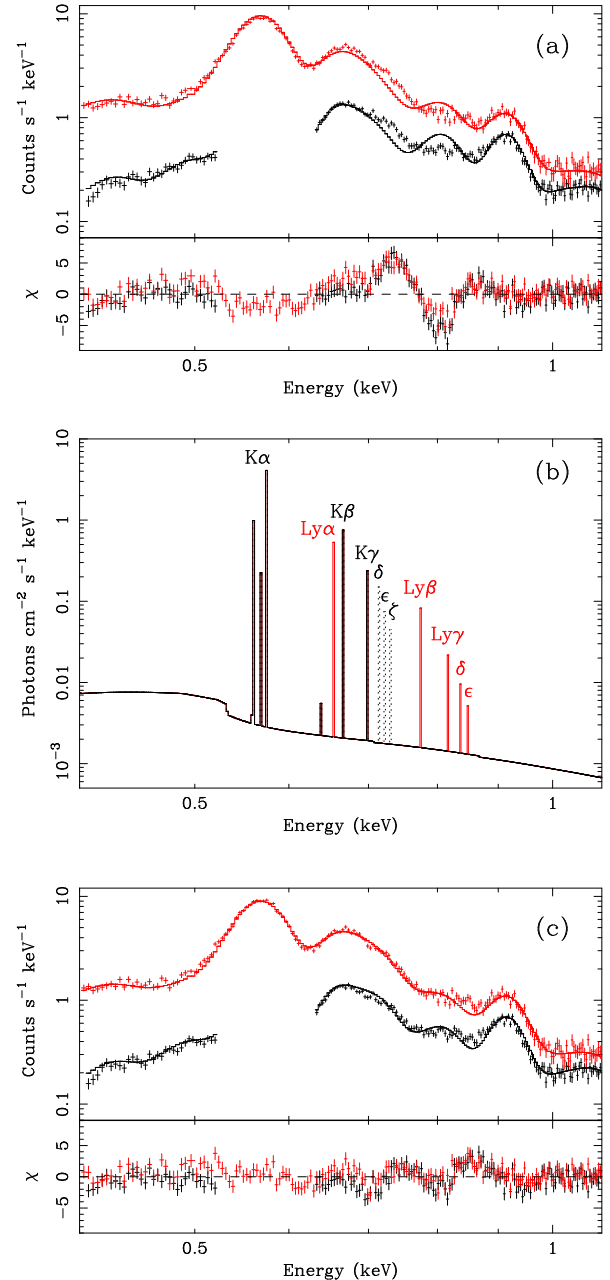


Fig. 5. (a) XIS spectra in the 0.4–1.1 keV band fitted with a VNEI model. The black and red data points represent the FI and BI spectra, respectively. (b) Spectrum in photon space corresponding to the model used in (a), but only showing O lines. It is binned every 2 eV. The black and red lines represent O VII series and O VIII series, respectively. The dotted lines are additional transitions of K δ (714 eV), K ϵ (723 eV), and K ζ (730 eV) of O VII added as separate Gaussians (see text). (c) Same spectra as (a), but for fits including Gaussians representing K δ (714 eV), K ϵ (723 eV), and K ζ (730 eV) of O VII (see text). The residuals in the energy band 0.7–0.85 keV seen in (a) are largely removed.

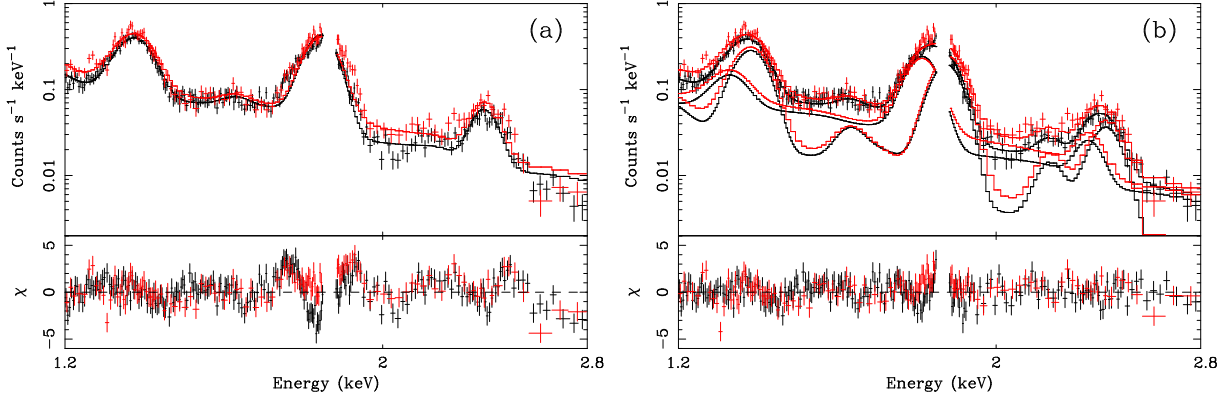


Fig. 6. (a) XIS spectra in the 1.2–2.8 keV band fitted with the one-component VNEI model. The black and red represent the FI and BI, respectively. (b) Same to (a), but fitted with the two-component VNEI.

agreement is not due to a calibration error, but is real.

If the intrinsic broadening of the Si-K α line (~ 40 eV; see table 1) is due to thermal Doppler broadening, the ion (silicon) temperature must be ~ 13 MeV, which requires a shock velocity of $\sim 1.5 \times 10^4$ km s $^{-1}$. Ghavamian et al. (2002) determined the shock velocity (from measurements of the H α line width) to be ~ 2900 km s $^{-1}$ in the NW portion of SN 1006. This is where the blast wave is interacting with significant amounts of interstellar matter, compared to other parts of the rim. In fact, the average size of the remnant (~ 15.5 radius) and the well-known age and distance allow us to determine a mean expansion speed for SN 1006 to be $\sim 10^4$ km s $^{-1}$. The true current blast wave speed in SN 1006 is almost surely bracketed by these two values. Furthermore, the reverse shock, which is likely to be the heating source for the Si that we see, typically moves into the ejecta at only a fraction of the blast wave speed. Therefore, we consider it unlikely that the line broadening we see is due to thermal Doppler broadening.

Another possible explanation proposes that the emission consists of several thermal plasma components. We fitted the spectra with 2-VNEI models, in which we allowed for different kT_e values, but the same $n_e t$ between components. However, no combination of parameters would fit the data, even if we let the abundances of Mg, Si, and S be free parameters. Not only 2-VNEI, but also 2-VPSHOCK models failed to fit the data when the two components were forced to have the same ionization timescale. All of the models that we tried, but rejected,

are summarized in table 2. The addition of a power-law component to these models also did not help to improve the fittings.

Next we tried two-component VNEI models with the same electron temperature, but different $n_e t$ values. The best-fit reduced χ^2 /d.o.f. was greatly improved to 401/346 (see table 2, for comparison). Models with different electron temperature and ionization timescale ($2-kT_e$ and $2-n_e t$) gave no significant improvement of the reduced χ^2 . We thus conclude that a 2-component VNEI model with different $n_e t$ values is necessary to fit the medium element plasma band. The best-fit parameters and spectra are given in table 3 and figure 6b, respectively.

5. Model Fit of the Full Band Spectra

In section 4, we discuss how we separately derived spectral parameters for the three-energy bands that represent typical plasma conditions for the main light elements (O and Ne), medium elements (Mg, Si, and S), and heavy element (Fe). A summary is given in table 4. We used these parameters as the initial values to search for plasma parameters in the full energy band of 0.3–10 keV; the resulting overall best-fit parameters must be consistent with the data over the entire XIS energy band.

Based on table 4, we assume that the model that describes the full spectral range must consist of, at least, three plasma components: (1) high- kT_e (~ 1 keV) with high- $n_e t$ ($\sim 10^{10}$ cm $^{-3}$ s), (2) similarly high- kT_e with low- $n_e t$ ($\sim 10^9$ cm $^{-3}$ s), and (3) low- kT_e (~ 0.6 keV) with medium- $n_e t$ ($\sim 7 \times 10^9$ cm $^{-3}$ s). First, we consider whether or not the full band spectra can be well reproduced with only these components. We also consider a broader range of kT_e and $n_e t$ values for the Fe-K emission.

As shown in table 3, components (1) and (2) are significantly enhanced in Mg, Si, and S (relative to solar). In the present spectral fits, we made the assumption that these components are composed purely of metals without any admixture of hydrogen or helium. This assumption

Table 2. Best-fit parameters and χ^2 values of the spectral fitting in the 1.2–2.8 keV band with the various models.

Model	kT_{e1} (keV)	kT_{e2} (keV)	$n_e t$ (cm $^{-3}$ s)	χ^2 /d.o.f.
1-VNEI	1.5	–	4.5×10^9	848/351
2-VNEI	0.18	20	8.4×10^9	706/346
1-VPSHOCK	1.6	–	8.3×10^9	726/351
2-VPSHOCK	0.36	12	1.0×10^{10}	597/346

Table 3. Best-fit parameters of the spectral fitting in the 1.2–2.8 keV band with 2-component VNEI model with different $n_e t$ values.

Parameter	Component 1	Component 2
N_H (cm $^{-2}$)	6.8×10^{20} (fixed)	
kT_e (keV)	1.1 (1.0–1.2)	
Mg	4.2 (3.5–5.2)	6.1 (3.5–13)
Si	19 (15–24)	15 (13–24)
S	24 (19–34)	23 (17–31)
$n_e t$ (cm $^{-3}$ s)	$1.3 (1.1\text{--}1.7) \times 10^{10}$	$7.9 (6.2\text{--}9.8) \times 10^8$
$n_H n_e V$ (cm $^{-3}$)	$2.8 (2.3\text{--}3.4) \times 10^{55}$	$1.9 (1.6\text{--}2.3) \times 10^{56}$
$\chi^2/\text{d.o.f.}$	401/346 = 1.16	

Table 4. Plasma components determined from the narrow band spectra.

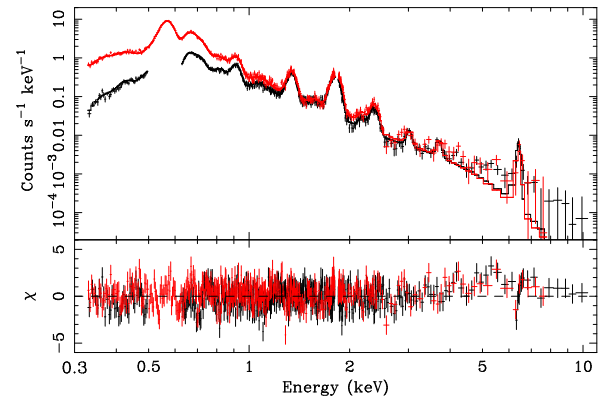
Band (keV)	Major elements	kT_e (keV)	$n_e t$ (cm $^{-3}$ s)	Component*
0.4–1.1	O, Ne	0.58 (0.56–0.59)	$6.7 (6.6\text{--}6.8) \times 10^9$	(3)
1.2–2.8	Mg, Si, S	1.1 (1.0–1.2)	$1.3 (1.1\text{--}1.7) \times 10^{10}$	(1)
		1.1 (1.0–1.2)	$7.9 (6.2\text{--}9.8) \times 10^8$	(2)
5.0–10	Fe	3.8 (1.7–26)	$6.1 (2.2\text{--}10) \times 10^9$	

*The plasma component identifications described in text.

arose because hydrogen and helium emit only continuum emission in the X-ray band. Given the complexity of our spectral model, it is just not possible with the XIS data to obtain reliable estimates for the level of continuum emission from the three plasma components separately. As a further assumption, we fixed the abundance of component (3) to be the solar value. (Anticipating the results given below, we found that most of the continuum emission above 1 keV actually comes from a hard power-law like spectral component.) Operationally, we fixed the oxygen abundance in both the pure-metal components (i.e., nos. 1 and 2) to a large value (1×10^4), and fitted for the abundances of other elements relative to oxygen. The C and Ni abundances were assumed to be the same as Ne and Fe, respectively. The emission measure (EM) in the plasma code is defined (in XSPEC) as $n_H n_e V$, even if the plasma is dominated by heavy elements. However, the oxygen density can be calculated as $n_O = (8.51 \times 10^{-4} n_H) \times 10^4$, where the numerical value is the solar abundance of oxygen from Anders and Grevesse (1989). Details of this method can be found in Vink et al. (1996).

Since the NEIvers 1.1 spectral model does not include K-shell emission lines from Ar and low ionization states of Ca, we added Gaussians at the energies of their $K\alpha$ transitions: 3.02 keV (Ar) and 3.69 keV (Ca) (see table 1). For component (1) we additionally freely varied the Ca abundance, which effectively allowed for the Ca L-shell lines to contribute at low energies (< 0.5 keV). For component (2), we tied the Ca abundance to that of Fe, which was allowed to vary freely. We also added Gaussians for the upper-level oxygen transitions at 0.714, 0.723, and 0.730 keV with the same reason as described in subsection 4.2.

We fitted the FI data in the energy band from 0.33 to 10 keV (0.33 to 8 keV for the BI data). We ignored the band below the C-edge at 0.28 keV, because of the large uncertainty in calibration due to contamination on the

**Fig. 7.** XIS spectra in the 0.33–10 keV band fitted with the three-component plasma model (see text). The black and red points represent the FI and BI data, respectively. The model fails to describe the continuum emission above ~ 4 keV.

OBF (see Koyama et al. 2007). Energies of 0.5–0.63 keV (only for FI) and 1.83–1.85 keV were also ignored for the same reasons as noted in subsections 4.2 and 4.3. Since the absolute gain of the XIS has an uncertainty of ± 5 eV (Koyama et al. 2007), we allowed for a small offset in the photon-energy to the pulse-height gain relationship.

With this model and assumptions, the best-fit $\chi^2/\text{d.o.f.}$ obtained was 1081/833. The fitted spectra are shown in figure 7. All line features are well fitted, even Fe-K, suggesting that including additional thermal components would not be justified. However, there is a systematic data excess in the continuum at energies $\gtrsim 4$ keV. We include a power-law component to model this, since we cannot reject the possibility that there is a non-thermal component here that is similar to the bright NE and SW rims (albeit much less intense). The fit with the additional power-law was significantly improved with $\chi^2/\text{d.o.f.} = 996/831$. The

Table 5. Best-fit parameters of the broadband spectral fitting.

Component	Parameter	Value
Absorption	N_{H} (cm^{-2})	6.8×10^{20} (fixed)
VNEI 1 (Ejecta 1)	kT_e (keV)	1.2 (1.1–1.4)
	Abundance (10^4 solar)	C 0.19* (0.08–0.30)
		N 0 (fixed)
		O 1.0 (fixed)
		Ne 0.19* (0.08–0.30)
		Mg 4.1 (3.7–4.7)
		Si 17 (15–20)
		S 23 (20–27)
		Ca 11 (9.6–13)
		Fe 0.68 [†] (0.62–0.76)
		Ni 0.68 [†] (0.62–0.76)
VNEI 2 (Ejecta 2)	$n_e t$ (cm^{-3} s)	$1.4 (1.2\text{--}1.6) \times 10^{10}$
	$n_{\text{H}} n_e V$ (cm^{-3})	$2.7 (2.4\text{--}3.0) \times 10^{51}$
	kT_e (keV)	1.9 (1.5–2.6)
	Abundance (10^4 solar)	C 0.33 [‡] (0.23–0.45)
		N 0 (fixed)
		O 1.0 (fixed)
		Ne 0.33 [‡] (0.23–0.45)
		Mg 3.0 (2.2–3.9)
		Si 10 (8.6–12)
		S 12 (9.1–16)
		Ca 18 [§] (5.1–44)
		Fe 18 [§] (5.1–44)
		Ni 18 [§] (5.1–44)
NEI (ISM)	$n_e t$ (cm^{-3} s)	$7.7 (6.7\text{--}9.2) \times 10^8$
	$n_{\text{H}} n_e V$ (cm^{-3})	$1.8 (1.3\text{--}2.5) \times 10^{52}$
	kT_e (keV)	0.51 (0.31–0.55)
	$n_e t$ (cm^{-3} s)	$5.8 (5.7\text{--}6.1) \times 10^9$
	$n_{\text{H}} n_e V$ (cm^{-3})	$1.1 (1.0\text{--}1.2) \times 10^{56}$
Power-law	Γ	2.9 (2.8–3.0)
	Norm (photons cm^{-2} s $^{-1}$)	$6.3 (5.5\text{--}7.2) \times 10^{-4}$
Gaussian lines to complement the incomplete VNEI code (see text)		
Line	Center Energy(keV)(fixed)	Norm (photons $\text{cm}^{-2}\text{s}^{-1}$)
O VII-K δ	0.714	$6.4 (6.1\text{--}6.6) \times 10^{-4}$
O VII-K ϵ	0.723	3.2×10^{-4} #
O VII-K ζ	0.730	1.6×10^{-4} **
Ar-K	3.01	$5.7 (4.4\text{--}7.0) \times 10^{-6}$
Ca-K	3.69	$2.4 (1.3\text{--}3.5) \times 10^{-6}$
Gain	Offset (eV)	−4.8
$\chi^2/\text{d.o.f.}$		996/831 = 1.20

*, [†], [‡] and [§] represent linked parameters.^{||}The differential flux at 1 keV.#Fixed to 50% of the normalization of O VII-K δ .**Fixed to 50% of the normalization of O VII-K ϵ .

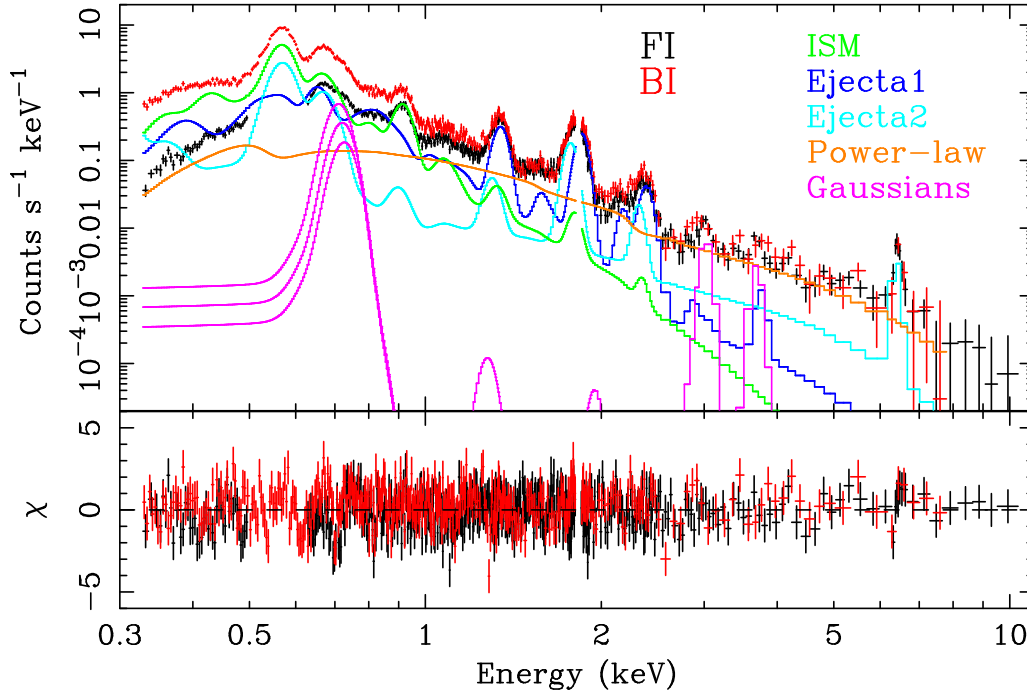


Fig. 8. XIS spectra in the 0.33-10 keV band which were extracted from the red elliptical region shown in figure 3. The black and red data points represent the FI and BI spectra, respectively. The solid lines, colored green, blue, light blue, orange, and magenta show the components of the ISM, Ejecta 1, Ejecta 2, Power-law, and additional Gaussians of the best-fit model for the BI spectrum. Note that the Gaussian like structures (magenta) at ~ 1.2 keV and ~ 1.9 keV are escape peaks of the added Gaussians at 3.02 keV and 3.69 keV due to the XIS response.

best-fit parameters are given in table 5. As already noted, the gain may have an uncertainty of ± 5 eV. The fitting process requires a gain offset of 4.8 eV for both FI and BI, within the allowable range. The best-fit model in the full energy band is shown in figure 8.

6. Discussion

In section 5, we analyzed the full energy band spectrum extracted from the elliptical region shown in figure 3, and found that it could be described adequately with a parameterized model including three thermal plasmas in non-equilibrium ionization (VNEI 1, VNEI 2, and NEI, in table 5) and one power-law component (Power-law, in table 5). Two of the plasmas, VNEI 1 and VNEI 2, were assumed to have non-solar abundances, and the other, NEI, was assumed to have solar composition. In the following we discuss the implications of our spectral results, but the reader is cautioned that these results are subject to change if the assumptions we have made are changed.

6.1. Origin of the Plasmas

The NEI model, assumed to have solar abundances, produces most of the observed low-energy X-rays, particularly the $K\alpha$ lines from O VII, O VIII, and Ne IX (see figure 8). This component is rather uniformly extended over the entire remnant, as can be seen in the O VII line band map (figure 1). We associate this component with the swept-up ISM.

The other plasmas, VNEI 1 and VNEI 2, with their non-solar elemental abundance ratios, are plausibly of ejecta origin. Since VNEI 1 has a larger ionization parameter than the other plasmas, we suggest that this plasma was heated by reverse shock in the early stage of remnant evolution (here Ejecta 1). On the other hand, VNEI 2 has an extremely low ionization parameter, and hence should have been heated much more recently (here Ejecta 2). We have firmly detected iron $K\alpha$ emission for the first time. The low ionization state of Fe, plus its overabundance in the Ejecta 2 component, is generally consistent with the Type Ia origin of SN 1006.

6.2. Relative Abundance in the Ejecta

We compare our best-fit relative abundances with the predicted nucleosynthesis yield of the widely-used W7 SN Ia model (Nomoto et al. 1984). For Ejecta 1, although the abundances of C, Ne, Mg, Si, and S relative to O are broadly consistent with the W7 model, Ca and Fe fall far below their predicted values, as shown in figure 9a. In the case of Ejecta 2, on the other hand, the heavy elements, albeit with large errors, are broadly consistent with the abundance pattern from the W7 model, as shown in figure 9b. These results, along with the difference in the ionization timescale between the components just mentioned, are consistent with a layered composition of the ejecta with the higher-Z elements more concentrated toward the center of SN 1006.

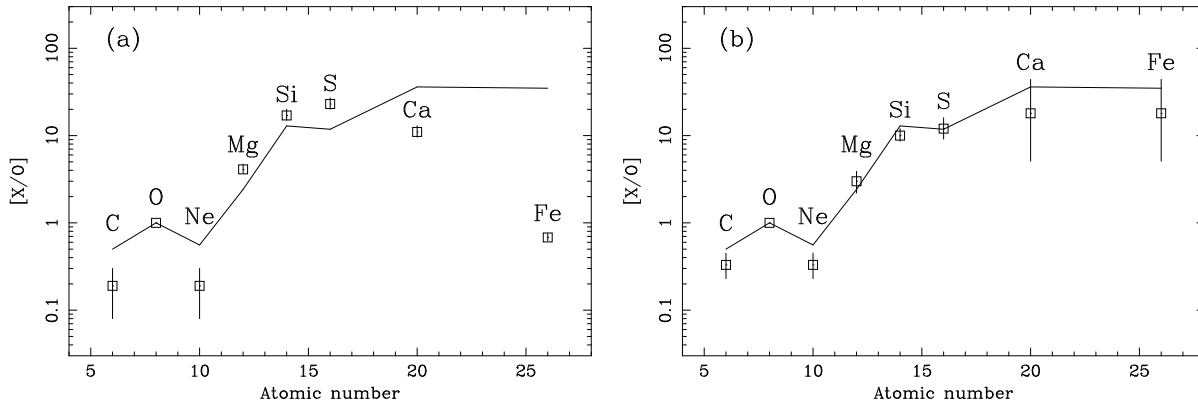


Fig. 9. Metal abundances as a function of atomic number derived from the spectral fitting. The data points of (a) and (b) represent those of Ejecta 1 and Ejecta 2, respectively. The solid lines show the abundance relative to oxygen calculated in the W7 model for a Type Ia supernova by Nomoto et al. (1984).

For this simple interpretation, one expects the Fe line emission from the low-ionization timescale component to be spatially located interior to the Mg and Si emission from the high-ionization component, i.e., near the center of SN 1006. As shown in figure 3, though, the Fe flux appears to peak close to the southeastern rim. In summary, our two-component spectral model for the ejecta is a highly simplified view of what is surely a complex multi- $n_e t$ and multi- kT_e structure that varies throughout the interior of the SNR. A longer observation, particularly of the inner regions of SN 1006, will help to improve the statistical accuracy of the Fe-K line flux, and allow us to study this apparent discrepancy in more detail.

6.3. ISM Density and Ion Temperature

The plasma parameters given in table 5 were derived from the southeast solid ellipse of figure 3, which is $\pi \times 6'.1 \times 4'.4 = 84 \text{ arcmin}^2$ in area. This corresponds to $3.3 \times 10^{38} \text{ cm}^2$, from which we estimated the emission volume to be $V = (3.3 \times 10^{38})^{3/2} = 6.0 \times 10^{57} \text{ cm}^3$. Therefore, the EM of the heated ISM derived from the spectral fits corresponds to an electron density of $n_e = 0.15 f^{-0.5} \text{ cm}^{-3}$, where f is the filling factor. Since the age of SN 1006 is $\sim 1000 \text{ yr}$, the ionization timescale can be roughly estimated as $n_e t \sim 4.7 \times 10^9 \text{ cm}^{-3} \text{ s}$, which is almost consistent with the best-fit value of the ionization parameter of the NEI (ISM) component. Such a low ionization age suggests that the temperatures of the ions and electrons may also be far from equilibrium. According to equation (3) of Laming (2001), under the assumption that the initial ratio between kT_e and kT_H just at the shock front is the ratio of the electron and proton masses, the proton temperature is estimated to be,

$$kT_H = 7.8 \left(\frac{n_e t}{5.8 \times 10^9 \text{ cm}^{-3} \text{ s}} \right)^{-1} \left(\frac{kT_e}{0.51 \text{ keV}} \right)^{5/2} [\text{keV}].$$

This result is consistent with that of the $H\alpha$ observation of $T_e/T_H \leq 0.07$ (Ghavamian et al. 2002). The extreme non-equilibrium state of the plasma is due to the low density

of the ambient medium. According to equations (2) and (5) of Ferrière (2001), the density of HI and HII at the Z -height of SN 1006 ($Z = 550 \text{ pc}$) is $\sim 0.03 \text{ cm}^{-3}$. This is consistent with our estimate of the ambient density of $n_H/4 \sim 0.03 \text{ cm}^{-3}$.

6.4. The Power-Law Component

The low density of the ambient medium will allow the velocity of the shock front to remain high for a relatively long time. This may be one reason why this remnant shows such efficient particle acceleration up to very high energies ($\sim 10^{14} \text{ eV}$), observed as power-law (synchrotron) emission from the NE and SW rims (Koyama et al. 1995). The photon index from these rims is $\Gamma \sim 2.7\text{--}2.9$. Now here, away from the bright rims, we also detect a power-law component in the hard energy band (the Power-law, in table 5) with a best-fit index of $\Gamma \sim 2.8\text{--}3.0$, which is consistent with the NE and SW bright rim emission. Since the power-law emissions from the rims are most likely to be synchrotron X-rays, the power-law component newly found from the ellipse in figure 3 is also likely to be synchrotron X-ray emission. The surface brightness is estimated to be $\sim 6 \times 10^{-15} \text{ ergs cm}^{-2} \text{ s}^{-1} \text{ arcmin}^{-2}$ in the 2–10 keV band. This value is ~ 50 -times lower than the peak emission at the NE and SW rims. If similar to the NE rim, the power-law component should show thin filamentary structures (Bamba et al. 2003). However, XMM-Newton (Rothenflug et al. 2004) and Chandra (Hughes et al., in preparation) observations found little evidence for filamentary X-ray rims along the SE rim.

7. Summary

We have analyzed high-quality spectra obtained with Suzaku of a region in the southern part of SN 1006, selected because it is bright in Fe-K α . The results and interpretations are summarized as follows:

1. The spectrum can be described by a model with at least three NEI thermal plasmas and one power-law

- component.
2. The fits yield different ionization parameters of $n_e t \sim 8 \times 10^8 \text{ cm}^{-3} \text{ s}$ (low), $\sim 6 \times 10^9 \text{ cm}^{-3} \text{ s}$ (medium), $n_e t \sim 10^{10} \text{ cm}^{-3} \text{ s}$ (high).
 3. The low- $n_e t$ plasma are highly overabundant in heavy elements, in which we found $K\alpha$ lines from Fe, for the first time. The abundance pattern is consistent with that of type Ia SN ejecta.
 4. The abundance of the medium- $n_e t$ plasma is assumed to be solar, and we associate this component with the shocked ISM. Although oxygen is not overabundant, $K\alpha$ lines of OVII and OVIII from this plasma appear to dominate the thermal emission from SN 1006. (However the complexity of our spectral model makes this claim less than definitive. We cannot exclude the possibility that the oxygen emission from this ISM component actually comes from yet another ejecta component. Spatially resolved spectroscopy would help to resolve this concern.)
 5. The high- $n_e t$ plasma is overabundant in medium elements, like Mg, Si, and S, but heavy element like Fe. Our interpretation is that this plasma also has an ejecta origin, and the composition is dominated by lower atomic number species.
 6. Temperature equilibrium between ions and electrons has not yet been achieved. The proton temperature of the shocked ISM is ~ 15 -times higher than the electron temperature.
 7. The spectrum from this region contains a power-law component. The photon index, $\Gamma \sim 2.9$, is similar to that of the northeast and southwest bright rims, suggesting that this component is also of synchrotron origin.

The authors thank all member of the Suzaku team, especially Y. Hyodo and H. Matsumoto. H.Y., S.K., H.N., and A.B. are supported by JSPS Research Fellowship for Young Scientists.

References

- Anders, E., & Grevesse, N. 1989, *Geochim. Cosmochim. Acta*, 53, 197
- Bamba, A., Yamazaki, R., Ueno, M., & Koyama, K. 2003, *ApJ*, 589, 827
- Bamba, A., et al. 2007, *PASJ*, 60 (# 3179)
- Decourchelle, A., et al. 2001, *A&A*, 365, L218
- Dubner, G. M., Giacani, E. B., Goss, W. M., Green, A. J., & Nyman, L.-Å. 2002, *A&A*, 387, 1047
- Ferrière, K. M. 2001, *Reviews of Modern Physics*, 73, 1031
- Ghavamian, P., Winkler, P. F., Raymond, J. C., & Long, K. S. 2002, *ApJ*, 572, 888
- Hamilton, A. J. S., Fesen, R. A., Wu, C.-C., Crenshaw, D. M., & Sarazin, C. L. 1997, *ApJ*, 481, 838
- Hwang, U., Hughes, J. P., & Petre, R. 1998, *ApJ*, 497, 833
- Ishisaki, Y., et al. 2007, *PASJ*, 59, 113
- Iwamoto, K., Brachwitz, F., Nomoto, K., Kishimoto, N., Umeda, H., Hix, W. R., & Thielemann, F.-K. 1999, *ApJS*, 125, 439
- Kokubun, M., et al. 2007, *PASJ*, 59, 53
- Koyama, K., Petre, R., Gotthelf, E. V., Hwang, U., Matsuura, M., Ozaki, M., & Holt, S. S. 1995, *Nature*, 378, 255
- Koyama, K., et al. 2007, *PASJ*, 59, 23
- Laming, J. M. 2001, *ApJ*, 546, 1149
- Long, K. S., Reynolds, S. P., Raymond, J. C., Winkler, P. F., Dyer, K. K., & Petre, R. 2003, *ApJ*, 586, 1162
- Masai, K. 1984, *Ap&SS*, 98, 367
- Mitsuda, K., et al. 2007, *PASJ*, 59, 1
- Nomoto, K., Thielemann, F.-K., & Yokoi, K. 1984, *ApJ*, 286, 644
- Rothenflug, R., Ballet, J., Dubner, G., Giacani, E., Decourchelle, A., & Ferrando, P. 2004, *A&A*, 425, 121
- Schaefer, B. E. 1996, *ApJ*, 459, 438
- Serlemitsos, P. J., et al. 2007, *PASJ*, 59, 9
- Takahashi, T., et al. 2007, *PASJ*, 59, 35
- Vink, J., Kaastra, J. S., & Bleeker, J. A. M. 1996, *A&A*, 307, L41
- Vink, J., Kaastra, J. S., Bleeker, J. A. M., & Preite-Martinez, A. 2000, *A&A*, 354, 931
- Vink, J., Laming, J. M., Gu, M. F., Rasmussen, A., & Kaastra, J. S. 2003, *ApJ*, 587, L31
- Wu, C.-C., Crenshaw, D. M., Fesen, R. A., Hamilton, A. J. S., & Sarazin, C. L. 1993, *ApJ*, 416, 247
- Warren, J. S., & Hughes, J. P. 2004, *ApJ*, 608, 261
- Winkler, P. F., Gupta, G., & Long, K. S. 2003, *ApJ*, 585, 324
- Winkler, P. F., Long, K. S., Hamilton, A. J. S., & Fesen, R. A. 2005, *ApJ*, 624, 189